

See discussions, stats, and author profiles for this publication at: <https://www.researchgate.net/publication/23177539>

# Quantitative (v, N, K(a)) product state distributions near the triplet threshold for the reaction $\text{H}(2)\text{CO} \rightarrow \text{H} + \text{HCO}$ measured by Rydberg tagging and laser-induced fluorescence

ARTICLE in THE JOURNAL OF PHYSICAL CHEMISTRY A · AUGUST 2008

Impact Factor: 2.69 · DOI: 10.1021/jp8021826 · Source: PubMed

CITATIONS

5

READS

22

11 AUTHORS, INCLUDING:



Hong-Ming Yin

Dalian Maritime University

39 PUBLICATIONS 509 CITATIONS

SEE PROFILE



Alexander Kai Buell

Heinrich-Heine-Universität Düsseldorf

47 PUBLICATIONS 745 CITATIONS

SEE PROFILE



Scott H Kable

University of New South Wales

148 PUBLICATIONS 2,291 CITATIONS

SEE PROFILE

# Quantitative ( $\nu$ , $N$ , $K_a$ ) Product State Distributions near the Triplet Threshold for the Reaction $\text{H}_2\text{CO} \rightarrow \text{H} + \text{HCO}$ Measured by Rydberg Tagging and Laser-Induced Fluorescence<sup>†</sup>

W. Scott Hopkins,<sup>‡,§</sup> Hans-Peter Loock,<sup>\*,‡</sup> Bríd Cronin,<sup>§,▽</sup> Michael G. D. Nix,<sup>§</sup> Adam L. Devine,<sup>§</sup> Richard N. Dixon,<sup>§</sup> Michael N. R. Ashfold,<sup>\*,§</sup> Hong-Ming Yin,<sup>⊥,+</sup> Steven J. Rowling,<sup>⊥</sup> Alexander Büll,<sup>⊥</sup> and Scott H. Kable<sup>\*,⊥</sup>

Department of Chemistry, Queen's University, Kingston, Ontario K7L 3N6, Canada, School of Chemistry, University of Bristol, Bristol BS8 1TS, U.K., and School of Chemistry, University of Sydney, NSW 2006, Australia

Received: March 12, 2008; Revised Manuscript Received: July 22, 2008

In this paper, we report quantitative product state distributions for the photolysis of  $\text{H}_2\text{CO} \rightarrow \text{H} + \text{HCO}$  in the triplet threshold region, specifically for several rotational states in the  $2^24^3$  and  $2^34^1$   $\text{H}_2\text{CO}$  vibrational states that lie in this region. We have combined the strengths of two complementary techniques, laser-induced fluorescence for fine resolution and H atom Rydberg tagging for the overall distribution, to quantify the  $\nu$ ,  $N$ , and  $K_a$  distributions of the HCO photofragment formed via the singlet and triplet dissociation mechanisms. Both techniques are in quantitative agreement where they overlap and provide calibration or benchmarks that permit extension of the results beyond that possible by each technique on its own. In general agreement with previous studies, broad  $N$  and  $K_a$  distributions are attributed to reaction on the  $S_0$  surface, while narrower distributions are associated with reaction on  $T_1$ . The broad  $N$  and  $K_a$  distributions are modeled well by phase space theory. The narrower  $N$  and  $K_a$  distributions are in good agreement with previous quasi-classical trajectory calculations on the  $T_1$  surface. The two techniques are combined to provide quantitative vibrational populations for each initial  $\text{H}_2\text{CO}$  vibrational state. For dissociation via the  $2^34^1$  state, the average product vibrational energy (15% of  $E_{\text{avail}}$ ) was found to be about half of the rotational energy (30% of  $E_{\text{avail}}$ ), independent of the initial  $\text{H}_2\text{CO}$  rotational state, irrespective of the singlet or triplet mechanism. For dissociation via the  $2^24^3$  state, the rotational excitation remained about 30% of  $E_{\text{avail}}$ , but the vibrational excitation was reduced.

## Introduction

Almost all organic species in the atmosphere of Earth degrade with a reaction pathway that includes formaldehyde ( $\text{H}_2\text{CO}$ ). Particularly in the upper atmosphere, chemistry occurs predominantly via photochemical processes. Aside from the atmospheric importance of  $\text{H}_2\text{CO}$ , its small size and character as the smallest carbonyl-containing species has made it a benchmark molecule in the study of photodissociation dynamics, both experimentally and theoretically. It is not possible here to summarize the extensive literature on  $\text{H}_2\text{CO}$  spectroscopy and photodissociation; below is a survey of the key results relevant to this study.

It has long been known that there are two chemical decomposition products following excitation of  $\text{H}_2\text{CO}$  to its first excited singlet ( $S_1$ ) state, simple bond cleavage to form the radical products  $\text{H} + \text{HCO}$  and the formation of molecular

products  $\text{H}_2 + \text{CO}$ .<sup>1</sup> However, even for a molecule as seemingly simple as  $\text{H}_2\text{CO}$ , it was noted recently in a Perspectives article in *Science* that “breaking up is never easy”.<sup>2</sup> This was a reference to the recent observation that each of these two chemical channels has two different mechanistic pathways. The molecular products can be formed either via a conventional transition-state (TS) mechanism or via a “roaming atom” mechanism.<sup>3</sup> Where there are two or more mechanistic pathways to product formation, prediction of relative rates and quantum yields is difficult and does not subscribe to simple kinetic theories such as TS theory. Indeed, the TS and roaming atom mechanisms have been shown to exhibit different energy dependences.<sup>4</sup>

The radical products can also be formed by two different mechanisms, decomposition via the ground state,  $S_0$ , or via the lowest triplet state,  $T_1$ . At wavelengths from 330 to 318 nm, internal conversion (IC) to  $S_0$  is dominant, and complete product state distributions (PSDs) have been measured for a wide variety of initial states in this region.<sup>5–7</sup> The main characteristic of all of these PSDs is that they are statistical. Phase space theory (PST) provides a satisfactory model of the HCO PSD across the  $N$ ,  $J$ ,  $K_a$ ,  $K_c$  set of rotational quantum numbers. This is just what would be expected from dissociation on a long-range, barrierless (except of centrifugal barrier) potential energy surface (PES).

At shorter wavelengths, Moore and co-workers first established the presence of the triplet channel by measuring a change in the H atom recoil velocity and bracketed its onset between

<sup>†</sup> Part of the “Stephen R. Leone Festschrift”.

\* To whom correspondence should be addressed. E-mail: hplloock@chem.queensu.ca (H.-P.L.); mike.ashfold@bris.ac.uk (M.N.R.A.); s.kable@chem.usyd.edu.au (S.H.K.).

<sup>‡</sup> Queen's University.

<sup>§</sup> University of Bristol.

<sup>⊥</sup> University of Sydney.

<sup>▽</sup> Current address: Department of Chemistry, University of Cambridge, Cambridge CB2 1EW, U.K.

<sup>+</sup> Current address: School of Chemistry, University of Oxford, Oxford OX1 3TA, U.K.

<sup>+</sup> Current address: State Key Laboratory of Molecular Reaction Dynamics, Dalian Institute of Chemical Physics, Dalian 116023, People's Republic of China.

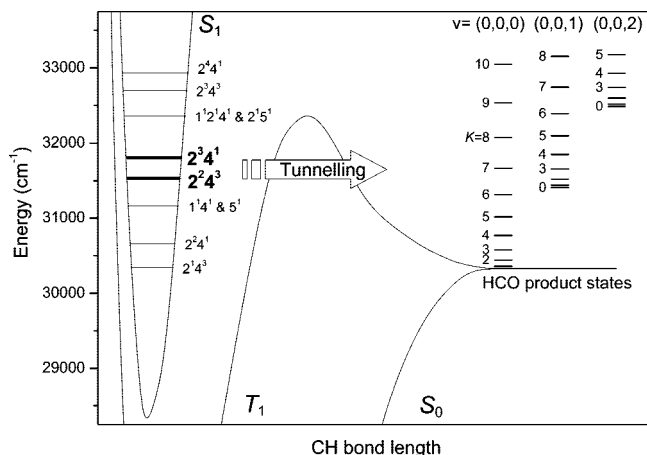


**Figure 1.** Schematic formaldehyde potential energy curves along the H–HCO coordinate of  $\text{H}_2\text{CO}$ . A representative set of available HCO product states is shown at the right.

308 and 319 nm ( $31350\text{--}32430\text{ cm}^{-1}$ ).<sup>8</sup> In this range, the translational, rotational, and vibrational energy partitioning deviates significantly from statistical, as shown in the H atom Rydberg tagging experiments of Wittig and co-workers.<sup>9,10</sup> The time-of-flight (TOF) spectra of Rydberg-tagged H atoms reveal the internal energy structure of the concomitant HCO fragment. Although quantitative PSDs could not be determined using this (then) relatively low resolution technique, the spectra very clearly showed some states with significant vibrational and rotational excitation, specifically in the  $K_a$  quantum number. Other nearby parent states, even within the same vibrational manifold, showed much colder HCO product internal energies. The interpretation of these observations was that  $\text{H}_2\text{CO}$  states that produced internally hot HCO reacted on the  $S_0$  surface, in agreement the previous studies at lower energy. States associated with cold HCO were attributed to reaction via the  $T_1$  channel, where little rotation and no vibrational excitation was expected on the basis of a late transition state on this PES.<sup>11</sup> The significant fluctuations in mechanism between nearby  $\text{H}_2\text{CO}$  states was attributed to tunneling on the  $T_1$  surface, which produces a broadened, but not continuum, set of background  $T_1$  states. This results in a fluctuating resonance between the  $S_1$  and  $T_1$  energy levels, competing with a weaker but consistent coupling to the dissociative  $S_0$  continuum.

A schematic representation of the potential energy surfaces in the spectral region of interest is shown in Figure 1. The spectral region between  $31000$  and  $33000\text{ cm}^{-1}$  is of particular interest since, here, the mechanism for H–CHO bond cleavage evolves from being dominated by the  $S_0$  pathway at the lower end of this range to being predominantly  $T_1$ -mediated at the upper end. The  $2_0^4 4_0^3$  ( $\bar{\nu}_0 = 31531.5\text{ cm}^{-1}$ ) and  $2_0^3 4_0^1$  ( $\bar{\nu}_0 = 31803.2\text{ cm}^{-1}$ ) transitions provide a particularly effective means of probing  $\text{H}_2\text{CO}$  photofragmentation mechanisms in this region as they have relatively large oscillator strengths and state-selectively populate the  $2^2 4^3$  and  $2^3 4^1$   $S_1$  vibronic levels (highlighted in Figure 1), both of which have shown evidence for competition between the IC- and intersystem crossing (ISC)-driven HCO formation.<sup>9,10,13</sup>

Quantitative measurement of H + HCO PSDs provides a rigorous benchmark against which theories and models of the two pathways can be judged. Previous LIF<sup>12</sup> and Rydberg tagging<sup>9,10,14</sup> studies have reported many aspects of the HCO product state distribution. These techniques are sensitive to different aspects of the PSDs; LIF experiments are very sensitive to the fine details of the  $N$ ,  $K_c$ , and  $J$  states and show  $N$

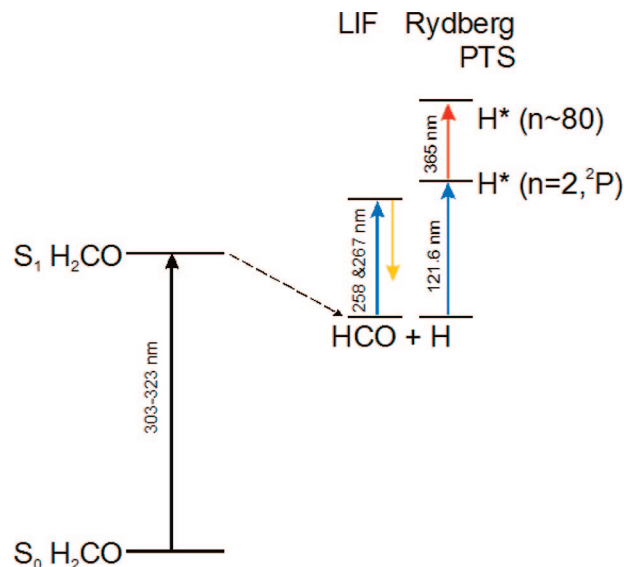


**Figure 2.** Parent excitation and product detection schemes.

distributions that are severely truncated in comparison to PST but which are modeled well by quasi-classical trajectory (QCT) calculations<sup>12</sup> for reaction on  $T_1$ . The  $K_c$  and  $J$  doublets are populated statistically. The LIF technique has difficulty measuring PSDs over  $v$  and  $K_a$  in HCO because of the diminishing quantum yield of fluorescence for higher-lying  $K_a$  and  $v$  states.<sup>15</sup> Rydberg tagging, on the other hand, reliably measures the  $v$  and  $K_a$  distributions and is unaffected by quantum yield issues but has more trouble resolving the finer  $N$ ,  $K_c$ , and  $J$  details. Recent high-resolution Rydberg tagging experiments have demonstrated resolution of the  $N$  states; however, the different  $K_a$  manifolds overlap, making quantitative extraction of PSDs over  $N$  difficult.

Recently, both of the groups involved in this paper became aware of each others work as two papers were published back-to-back.<sup>13,14</sup> We noticed that many of the initially prepared  $\text{H}_2\text{CO}$  parent states were common to both studies, and therefore, we decided to pool all of our data in this region, both published and unpublished. Comparison of the data allowed the weaknesses in one technique to be scaffolded by the strengths of the other. The result is that we can provide the quantitative, complete PSDs ( $v$ ,  $N$ ,  $K_a$ ,  $K_c$ ,  $J$ ) and determine the average energy disposed into vibrational, rotational, and translational energy for HCO in this interesting and challenging triplet threshold region of  $\text{H}_2\text{CO}$  photochemistry.

## Experimental Section

Both LIF and Rydberg tagging experiments have been described in detail in recent publications.<sup>13,14</sup> A summary of the pump and probe schemes is shown in Figure 2.

The H (Rydberg) atom photofragment translational spectroscopy (PTS) studies were performed using the experimental methodology and apparatus described in refs 16 and 17 with a slit-shaped mask placed in front of the ion detector.<sup>14</sup> Three laser beams were spatially overlapped in the center of the interaction volume, where they intercept a skimmed, pulsed, molecular beam of formaldehyde, seeded in argon. Nascent H atoms produced from  $\text{H}_2\text{CO}$  photolysis were excited in a two-photon, double resonance excitation scheme. The first photon (121.6 nm from frequency tripling 364.7 nm in Kr/Ar) excited the  $n = 2$ ,  $2p$  level; then, the second photon ( $\sim 365$  nm) further excited the H atoms to a high- $n$  Rydberg state ( $n \approx 80$ ) (see

Figure 2). “Rydberg-tagged” H atoms with recoil velocities along the TOF axis traveled under collision-free conditions to the detector (Johnston multiplier, type MM1-SG) where they were field ionized and their time of arrival recorded. Unwanted  $H^+$  ions formed by 121.6 plus 364.7 nm absorption were extracted by applying a potential (50 V  $cm^{-1}$ ) between a pair of annular electrodes positioned normal to the TOF axis above and below the interaction volume.

Paraformaldehyde (prilled) was obtained commercially (Aldrich, 95%) and packed into a 7  $\mu m$  stainless steel inline filter (Swagelok). Dried  $MgSO_4$  was placed in a second filter further downstream, and both chemicals were kept in place with glass wool plugs. The filters were arranged behind the pulsed nozzle, and the assembly was heated to  $\sim 70$  °C. Upon heating, the paraformaldehyde liberated monomeric formaldehyde and water. The  $MgSO_4$  acted as a desiccant to absorb the water and to stop the nozzle from clogging. Ar ( $\sim 2$  bar) was passed through the filters and the pulsed valve to form a pulsed supersonic expansion of  $H_2CO$ .

The laser-induced fluorescence (LIF) setup and conditions were similar to those used previously.<sup>5,13</sup> A jet of formaldehyde was created in the same way as that in the Rydberg tagging experiments above, although He was used as the carrier gas. Crossing the central region of the expansion, about 10 mm downstream, were two mutually orthogonal unfocused laser beams, to photolyze  $H_2CO$  at  $\lambda \sim 320$  nm and to probe the nascent HCO fragments by LIF at  $\sim 258$  or  $\sim 267$  nm (see Figure 2). The probe laser pulse was delayed with respect to the photolysis laser by 50–100 ns to discriminate against scattered pump light while maintaining collision-free conditions. LIF from the intersection of the laser beams was imaged onto the slits of a small monochromator (20 nm bandpass) and detected with a photomultiplier tube. The signal from the PMT was passed to a gated integrator and boxcar averager and then to a computer.

## Results and Analysis

Figure 3 shows representative experimental data obtained following population of the same initial state of  $H_2CO$ , that is, the  $2^2A'$  ( $1_{0,1}$ ) state excited at  $31518.4$   $cm^{-1}$ . Figure 3a shows a LIF spectrum of the  $0_0^0$  and  $3_1^1$  bands of the  $HCO(\tilde{B} \leftarrow \tilde{X})$  transition, which probes the production of  $v_3 = 0$  and 1 HCO, respectively. Figure 3b shows a HCO internal energy spectrum obtained using the H atom Rydberg tagging technique. In both cases, the fits to the measured spectra used to extract population distributions are shown below the spectra.

**H (Rydberg) PTS Analysis Method.** H atom TOF spectra recorded after dissociation of the H–CHO bond were analyzed in terms of total kinetic energy release (TKER) for the system. The quantized nature of the formyl radical internal energies is directly correlated to the H atom kinetic energies. Therefore, the H atom TOFs,  $t_H$ , are constrained to values reflecting the HCO rovibrational distributions throughout the available energy space.

The TKER can be defined in terms of  $t_H$  by

$$TKER = \frac{1}{2} m_H \left( 1 + \frac{m_H}{m_R} \right) \left( \frac{d}{t_H} \right)^2 \quad (1)$$

where  $d$  is the distance between the laser interaction region and the detector and  $m_H$  and  $m_R$  are the masses of the H atom (1.0078 amu) and the HCO partner fragment (29.018 amu), respectively. With TKER obtained from the experiment, the internal energy,  $E_{int}$ , of the HCO fragment can then be established using conservation of energy arguments

$$E_{int} = E_{phot} - TKER - D_0(H-CHO) \quad (2)$$

where  $E_{phot}$  is the photon energy and  $D_0(H-CHO) = 30327.6$   $cm^{-1}$ .

Using documented HCO molecular parameters,<sup>18</sup> a stick spectrum of HCO term energies was generated to facilitate assignment of the HCO internal energy spectrum. Each line was then given a line width of  $\sim 2$   $cm^{-1}$  (Gaussian, fwhm), and the spectrum was converted to a TKER spectrum for direct comparison with the measured H atom TOFs. Simulated line intensities were then adjusted to approximately reproduce those of the experimental spectrum using a Gaussian distribution for the  $K_a$  stacks (illustrated on the right side of Figure 1) and a second Gaussian distribution for the  $N$ -level populations within each  $K_a$  stack. To fit the simulated spectrum to the experimental data, a gradient descent method was used to minimize least-squares errors as a function of the mean and standard deviation in the widths of the  $N$  and  $K_a$ , envelopes, the spectral line width, and a small term to account for spectral term energy offset. The integrated spectral intensity was then normalized such that PSDs could be extracted for each rotational level. Since there was no physical reason to assume that the spectral line intensity distributions should be described by Gaussian analytical functions of  $N$  and  $K_a$ , each of the line intensities in the predicted spectrum was then adjusted manually to reduce the fit residuals further. Each manual fit was repeated three times as a means of estimating reproducibility.

**LIF Analysis Method.** The  $\tilde{B} \leftarrow \tilde{X}$  transition in HCO is a hybrid  $a/b$  transition, which yields nine rotational branches. Most

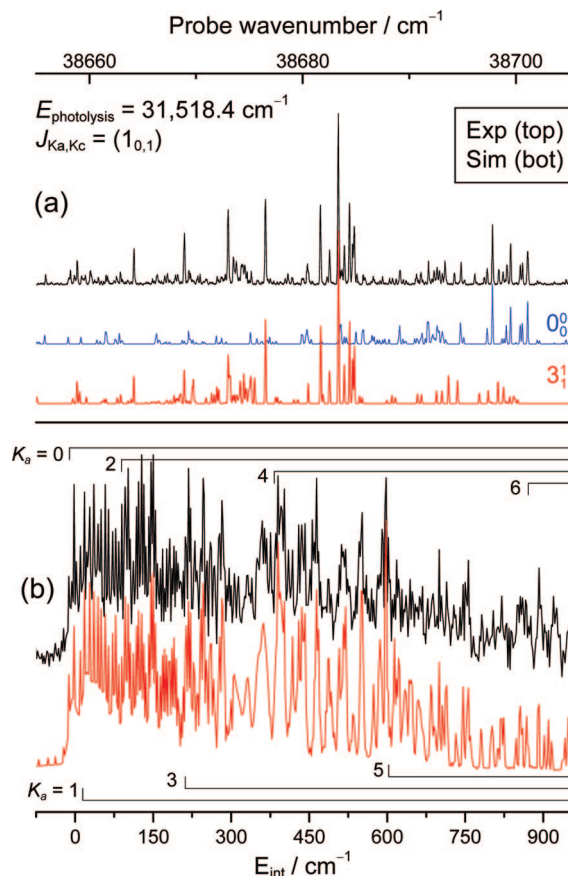


**Figure 3.** (a) LIF spectra of the HCO ( $v = 0$  and  $v_3 = 1$ ) products and (b)  $E_{int}$  spectrum of HCO obtained by H atom Rydberg tagging. Both experiments were performed following excitation of  $H_2CO$  to the  $2^2A'$  ( $1_{0,1}$ ) state at  $31518.4$   $cm^{-1}$ . In each case, model spectra are shown below the experimental data.



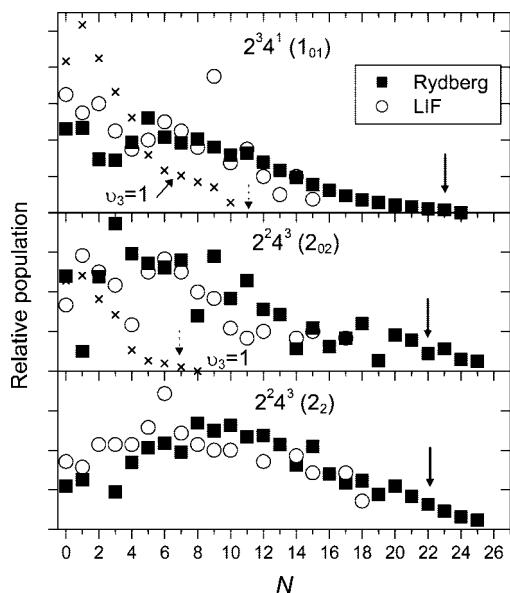


**Figure 4.** HCO  $N$  distributions ( $v = 0$  and  $v_3 = 1$ ,  $K_a = 0$ ) for the three initial  $\text{H}_2\text{CO}$  states indicated. (Top)  $T_1$ -mediated PSDs. (Bottom)  $S_0$ -mediated PSDs. (Center) PSDs where both  $S_0$  and  $T_1$  mechanisms are active. Arrows mark the population limit allowed by the conservation of energy and angular momentum (solid arrow,  $v = 0$ ; dashed arrow,  $v_3 = 1$ ).

individual product states had at least one of these nine transitions that were largely free from overlap. The spectral simulation in Figure 3a uses published rotational constants for the  $\tilde{X}(0,0,1)$  and  $\tilde{B}(0,0,0)$  states of HCO.<sup>19–21</sup> The spectral line positions were calculated using Sears's ASYTOP program.<sup>22</sup> The spectral intensities were then simulated using the known  $N$ ,  $K_a$ ,  $K_c$ ,  $J$  specific line strengths, including effects of asymmetry splitting, spin–rotation splitting, and axis switching.<sup>23</sup> The intensities were also scaled for the individual state-specific fluorescence quantum yields.<sup>15</sup> This whole process has been described in detail previously.<sup>6,7</sup> The relative population in each ( $v$ ,  $N$ ,  $K_a$ ,  $K_c$ ,  $J$ ) state was varied until the best simulation of the experimental spectrum of the nascent HCO fragments was found. Our strategy was to start fitting nonoverlapped transitions with  $K_a'' = 0$  while retaining all other (partially overlapped) branches in the simulated spectrum.  $K_a'' = 1$  and 2 transitions were added sequentially. Populations were then adjusted iteratively until the best agreement in the intensities of all branches was obtained. The simulation overlapping the experimental spectrum is quantitative and yields an excellent fit to the data.

**Rotational State Distributions and Average Rotational Energy ( $v = 0$ ).** Figure 4 shows representative PSDs over the  $N$  states of HCO ( $N$  is the overall rotation of HCO, excluding electron spin) following population of three different initial  $\text{H}_2\text{CO}$  states. The PSD in the lowest panel is clearly broader than that in the top panel, despite having less available energy. Broad  $N$  distributions are indicative of reaction on the barrierless  $S_0$  PES.<sup>7,13</sup> On the other hand, the narrower distribution, shown in the top panel, peaks at very low  $N$  and is characteristic of reaction on the  $T_1$  PES.<sup>13</sup> The center panel shows characteristics of both mechanisms, high population at very low  $N$  but population that continues to the limit allowed by energy and angular momentum conservation (indicated by a vertical arrow in each of the panels in Figure 4). The most impressive feature, however, is the remarkable agreement between results obtained by two completely different experimental techniques. The LIF method resolves every different HCO state but suffers from

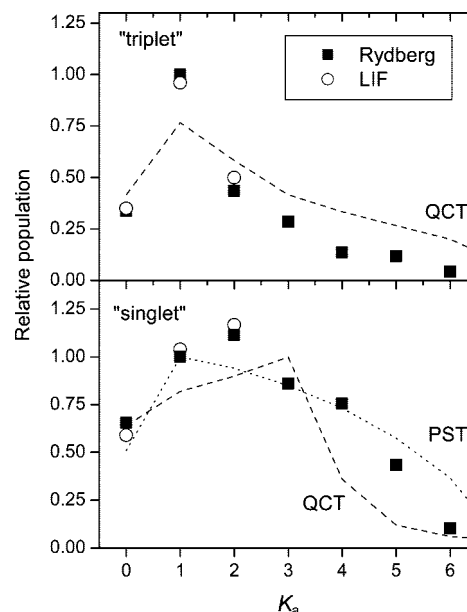


**Figure 5.** HCO  $K_a$  population distributions for  $v = 0$ . (Top)  $T_1$ -mediated PSDs observed following excitation to the  $\text{H}_2\text{CO}$   $2^3 4^1 (1_{01})$  level. (Bottom)  $S_0$ -mediated PSDs observed following excitation to the  $\text{H}_2\text{CO}$   $2^2 4^3 (2_2)$  levels. The prediction of two theoretical models is shown for comparison (see text).

complex HCO spectroscopy, in which the detection sensitivity of every HCO state is different, and needs to be corrected for. The Rydberg tagging experiments are pushing the limit of experimental resolution for this technique. Individual  $N$  states are typically not resolved, but the energy distribution is absolute and unaffected by variation in spectroscopic intensities. In general terms, therefore, the Rydberg tagging distributions are more reliable for the overall distribution, while the LIF populations are better for resolution of finer details. In each case, the two techniques produce near-quantitative agreement for each  $N$  distribution.

Previous studies, both experimental<sup>6–13</sup> and theoretical,<sup>12</sup> indicate that the  $K_a$  population distribution should discriminate effectively between  $S_0$  and  $T_1$  channels. LIF experiments are only sensitive to low  $K_a$  because the quantum yield for fluorescence drops significantly for increasing  $K_a$ .<sup>15</sup> Rydberg tagging experiments, on the other hand, are sensitive to total energy. TKER spectral intensities are a direct measurement of the rovibrational energy distribution of the HCO cofragment; however, since high-lying  $N$  states for low  $K_a$  stacks overlap low-lying  $N$  for higher  $K_a$  stacks, ambiguity is introduced. Nevertheless, comparison of the  $N$  distributions extracted from the TKER spectra with those determined from the LIF data (Figure 4) demonstrates that the fitting procedure described above is robust. Therefore, we expect that the  $K_a$  distributions extracted in the same way are also robust. Figure 5 shows two such  $K_a$  distributions. The lower panel shows a broad distribution that extends to the limit of available energy, while the upper panel shows a much shorter distribution with little population for  $K_a > 2$ . For comparison, the same populations derived from the LIF studies (from which data for  $K_a \leq 2$  only can be extracted) are also shown. The agreement again is excellent. Phase space theory<sup>24</sup> has been shown to model the HCO  $N$  distribution and the  $K_a$  distribution up to  $K_a = 2$  for reactions via the  $S_0$  PES.<sup>6,7</sup> The PST prediction for the  $K_a$  distribution in the lower panel in Figure 5 is in good agreement with the broad PSD for all  $K_a$  up to the limit of energy conservation, clearly identifying a broad  $K_a$  distribution as representative of reaction

on  $S_0$ . The short  $K_a$  distribution, by analogy with the narrower  $N$  distribution in Figure 4, is associated with the  $T_1$  PES.

Quasi-classical trajectory calculations, run on a high-quality *ab initio* PES, have been reported previously for  $S_0$  and  $T_1$  pathways in this threshold energy region.<sup>12</sup> Two of the QCT results have been reproduced and scaled to the experimental results in Figure 5. The QCT  $K_a$  distribution from the  $T_1$  surface shows a peak at  $K_a = 1$  and a population that tails to zero for higher  $K_a$ . The experimental results peak more sharply, with a steeper decay; however, the overall form of the distribution is captured faithfully by the theory. The QCT distribution for the singlet channel is broader, with significant population extending through  $K_a = 3$  and then dropping for higher  $K_a$ . The experimental PSD peaks a little earlier and is populated more strongly out to the maximum  $K_a$  allowed by energy conservation. Given the large number of trajectories reported, this difference should not be one of statistics but, rather, be a reflection of differences between the true and *ab initio* PES.

The average energy deposited into each degree of freedom of reaction products provides a useful indicator of the reaction dynamics. Such averages have not been reported before for  $H_2CO$  dissociation because only incomplete or nonquantitative PSDs have been reported to date. To calculate the average energy deposited into rotational degrees of freedom, the population in each rotational state ( $N$ ,  $K_a$ ) was multiplied by its respective term energy. Summing these fractional internal energies yielded the average rotational excitation for the  $v = 0$  products

$$\langle E_{v=0}^{\text{rot}} \rangle = \sum_{N,K_a} [P_{N,K_a,v=0}] [E_{N,K_a,v=0}^{\text{rot}}] \quad (3)$$

where  $P_{N,K_a,v=0}$  is the fractional population of each ( $N$ ,  $K_a$ ,  $v = 0$ ) state and  $E_{N,K_a,v=0}^{\text{rot}}$  is the associated rotational energy. Table 1 lists the fraction of available energy deposited as HCO ( $v = 0$ ) rotational energy for all initial states in this study. The  $\langle E_{\text{rot}} \rangle / E_{\text{avl}}$  ratio generally lies in the range of 0.24–0.30, but a few initial states, associated with the singlet pathway, yield higher ratios, and two states (triplet pathway) yield significantly lower ratios.

**Vibrational State Distributions and Average Vibrational Energy.** The  $v_3 = 1$  state of HCO is also energetically accessible following photodissociation from the  $2^2A_3$  state, as shown in Figure 3a. In principle, the same process for rotational PSDs could be extended to the  $v_3 = 1$  products, but in practice, it was not possible to extract reliable quantum-state-resolved populations from the Rydberg tagging experiments because of the very low H atom kinetic energies. However, we were able to estimate the fraction of the total HCO population formed in the  $v_3 = 1$  state following excitation via the  $2^3A_1$  state by integrating the measured PTS signal at energies below the maximum KE associated with  $H + HCO$  ( $v_3 = 1$ ) products and comparing it with the total signal. The average vibrational populations determined in this way are summarized in Table 1. With one exception, the  $\langle E_{\text{vib}} \rangle / E_{\text{avl}}$  ratio for the  $2^3A_1$  state lies between 0.11 and 0.16. This exception corresponds to the  $H_2CO$  state that is strongly coupled to the triplet manifold.

Accurate rotational populations for  $v_3 = 1$  can, however, be measured via LIF, as published previously.<sup>13</sup> However, scaling the specific rotational populations in  $v = 0$  to  $v_3 = 1$  was problematic and associated with large errors. In addition, overall vibrational populations were not obtained because not all  $K_a$  states in  $v = 0$  could be measured. The Rydberg data, however, can provide a calibration for the LIF data, and as a consequence, the LIF data can then provide accurate relative rotational and vibrational populations in both  $v = 0$  and  $v_3 = 1$ .

**TABLE 1: Partitioning of Available Energy Following Photolysis of Formaldehyde via Selected Levels of the  $\tilde{A}^1A_2$  Excited Electronic State<sup>a</sup>**

photolysis wavenumber ( $\text{cm}^{-1}$ )	$H_2CO \tilde{A}^1A_2$ excited state(s)	$\langle E_{\text{rot}} \rangle / E_{\text{avl}}$	$\langle E_{\text{vib}} \rangle / E_{\text{avl}}$	mechanism <sup>b</sup>
31 829.0	$2^3A_1 (2_{2,0}) + (2_{2,1})$	0.28	0.16	
31 814.5	$2^3A_1 (4_{1,4})$	0.28	0.15	
31 812.8	$2^3A_1 (1_{1,1})$	0.24	0.12	
31 810.5	$2^3A_1 (1_{1,0})$	0.13	0.07	T
31 798.0	$2^3A_1 (3_{0,3})$	0.28	0.11	
31 794.5	$2^3A_1 (1_{0,1})$	0.24	0.13, 0.10.136 <sup>c</sup>	
31 793.5	$2^3A_1 (2_{0,2})$	0.26	0.13, 0.12 <sup>c</sup>	
31 556.0	$2^2A_3 (3_{2,1}) + (3_{2,2}) + (4_{1,3})$	0.32(8)	n/a	S
31 555.0	$2^2A_3 (2_{2,0}) + (2_{2,1})$	0.32(7)	0.12 <sup>c</sup>	S
31 544.0	$2^2A_3 (3_{1,3}) + (4_{1,4})$	0.27(7)	n/a	
31 542.2	$2^2A_3 (2_{1,2})$	0.27(4)	n/a	
31 540.5	$2^2A_3 (1_{1,1})$	0.19(4)	n/a	T
31 538.2	$2^2A_3 (1_{1,0})$	0.32(6)	n/a	S
31 533.2	$2^2A_3 (1_{1,1})$	0.28(5)	n/a	
31 522.9	$2^2A_3 (1_{0,1})$	0.29(7)	0.11 <sup>c</sup>	
31 522.1	$2^2A_3 (2_{0,2})$	0.25(8)	0.09 <sup>c</sup>	
31 520.9	$2^2A_3 (0_{0,0}) + (3_{0,3})$	0.30(8)	n/a	S
31 518.4	$2^2A_3 (1_{0,1})$	0.29(6)	n/a	

<sup>a</sup> States indicated by “T” are those identified as dissociating predominantly via the  $T_1$  channel, as reflected by the  $\langle E_{\text{rot}} \rangle / E_{\text{avl}}$  and  $\langle E_{\text{vib}} \rangle / E_{\text{avl}}$  ratios. States indicated by “S” are considered to dissociate predominantly via the  $S_0$  product channel, while both mechanisms are deduced to make significant contributions to the decay of the unlabeled states. <sup>b</sup> S = singlet; T = triplet. <sup>c</sup> From recalibrated LIF measurements (see text).

The calibration is performed in two steps. First, the complete  $v = 0$  rotational distribution afforded by Rydberg tagging is used to provide the fraction of the overall rotational population that has  $K_a = 0$ . For example, in the data at the top of Figure 4 ( $2^3A_1 (1_{01})$ ), the  $K_a = 0$  population is 11% of the total rotational population. Second, LIF experiments can yield accurate rotational distributions within  $v_3 = 1$ ,<sup>13</sup> which can be scaled to the  $v = 0$ ,  $K_a = 0$  populations using estimated Franck–Condon (FC) factors. Using  $2^3A_1 (1_{01})$  again as an example, the total  $v_3 = 1$  population was estimated by LIF to be 2.4 times the population of  $v = 0$ ,  $K_a = 0$ .<sup>13</sup> Multiplying these two results provides the ratio of population in each vibrational state estimated from LIF,  $P(v_3 = 1)/P(v = 0) = 0.26$ . The purely Rydberg tagging result for the  $2^3A_1 (1_{01})$  state, but without resolution of the internal state distribution, is  $P(v_3 = 1)/P(v = 0) = 0.22$ . It should be recognized that the Rydberg tagging result is likely to be an underestimate because Rydberg tagging cannot measure the very slowest H atoms, which are more likely to arise in concert with vibrationally excited HCO. The agreement between these results is well within the mutual uncertainties of the two methods. For example, the major uncertainty in the LIF measurement is the estimated FC factor, with a quoted uncertainty of 50%.<sup>13</sup>

The Rydberg tagging data can now be employed as a calibration factor for LIF (providing, essentially, an indirect but experimental measurement of the FC factor). An example of the recalibrated rotational populations from LIF is shown overlapping the  $v = 0$  data in Figure 4. The populations in  $v_3 = 1$  are equal to or somewhat higher than  $v = 0$  for low  $N$ ; however, the restricted available energy, shown as a dashed

arrow in the figure, decreases the population significantly for higher  $N$ . This analysis also provides a concrete explanation for the apparent discrepancy between previous LIF and Rydberg tagging observations. Rydberg tagging data indicated that HCO vibrational excitation from the triplet pathway was very modest, while LIF data indicated the vibrational population was significant. We can now assert that the methods are consistent but measure different aspects of the vibrational population. Rydberg tagging provides the overall excited vibrational population (17% for this state), while the LIF is sensitive to population in individual rotational states, which, as shown in Figure 4, can be as significant as that for  $v = 0$ . The difference lies in the significantly fewer rotational levels available for the  $v_3 = 1$  level compared to  $v = 0$ . For the  $2^3 4^1$  state under discussion here, there are  $\sim 600$  energetically accessible ( $N$ ,  $K_a$ ,  $K_c$ ,  $J$ ) rotational states of  $v = 0$ , whereas there are only  $\sim 160$  such product states available within  $v_3 = 1$  (see Figure 1 for an illustration of the  $K_a$  density of states associated with each vibration). Once again, this highlights the relative strengths of each detection technique, with Rydberg tagging providing an overall picture of the product vibrational population that is unavailable to LIF and LIF providing the state-specific rovibrational populations that cannot be resolved with Rydberg tagging.

The calibration factor for the LIF vibrational populations is universal. The same scaling can be applied to all LIF data in ref 13; all  $v_3 = 1$  populations in that work should therefore be scaled down by 1.3. As mentioned above, the  $2^2 4^3$  state is close to the threshold for producing  $v_3 = 1$  HCO, and therefore, the H atom recoil velocity is too slow for Rydberg tagging to provide any measurement of vibrational population. Three of the set of  $2^2 4^3$  rotational states in Table 1 have also been probed by LIF. The newly calibrated LIF data can now be used to provide quantitative vibrational populations and average energies,  $\langle E_{\text{vib}} \rangle / E_{\text{avil}}$ , for these states, which are indicated in the table. The average vibrational population ratios are smaller than those from dissociation via the  $2^3 4^1$  state, even though the average rotational energy in the products is similar.

**Singlet and Triplet Pathways.** The  $S_0$  and  $T_1$  dissociation pathways have been shown previously to exhibit different dynamical signatures,<sup>9,10</sup> which are manifested by different PSDs. Internal conversion leads to randomization of parent internal energies on the  $S_0$  surface prior to dissociation, thereby favoring “statistical” quantum state population distributions in the photofragments. In contrast, products formed as a result of coupling to the quasi-bound  $T_1$  PES have higher KEs and hence lower internal vibrational and rotational excitation.<sup>10,12</sup> States in Table 1 with the highest measured fraction of internal energy (i.e., high  $\langle E_{\text{rot}} \rangle / E_{\text{avil}}$  and/or  $\langle E_{\text{vib}} \rangle / E_{\text{avil}}$ ), labeled “S” in the table, have been shown to exhibit statistical PSDs in both  $N$  (ref 13) and  $K_a$  (this work). We can therefore attribute the measured fraction of rotational energy for these states ( $\sim 30\%$ ) as being representative of the internal energy deposited via reaction on the  $S_0$  PES. PSDs (over  $N$  previously and  $K_a$  in this work) from states with the lowest fractions of internal energy, labeled “T” in the table, have been shown to be consistent with previous QCT calculations for reaction purely on the triplet surface, and therefore, a product rotational energy of  $\sim 15\%$  of the available energy can be taken as representative of triplet dynamics.

Intermediate fractions therefore suggest participation of both  $T_1$  and  $S_0$  mechanisms and might, with further investigation, provide a means of determining the  $S_0/T_1$  branching ratio for individual initial states. For example, it is interesting to note that the states identified as reacting solely via  $S_0$  are all

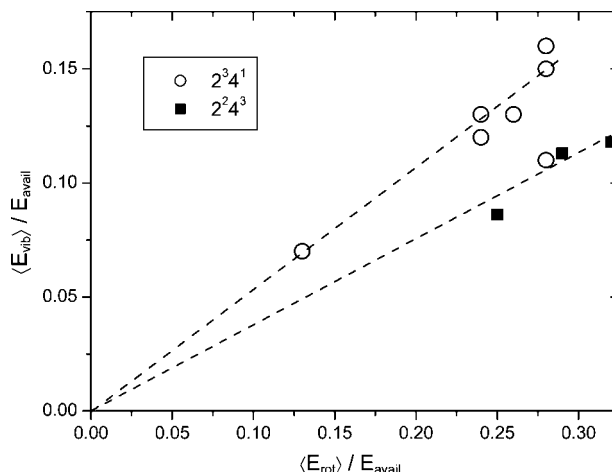


**Figure 6.** Correlation between the fraction of available energy distributed into HCO rotational energy and vibrational energy. The arrow joining the two data points indicates the same initial state measured by LIF and Rydberg tagging.

associated with the (lower energy)  $2^2 4^3$  vibrational level; all of the investigated rotational states in the higher-lying  $2^3 4^1$  level are deduced to dissociate, at least in part, by coupling to the  $T_1$  PES. The average  $\langle E_{\text{rot}} \rangle / E_{\text{avil}}$  measured for dissociation via the  $2^2 4^3$  state is 0.29, while that for dissociation via  $2^3 4^1$  is 0.24, again pointing to a stronger triplet presence in the higher-lying  $2^3 4^1$  state. Such conclusions accord with our, and previous,<sup>9,10,14</sup> expectations that  $T_1$ -mediated dissociation becomes dominant once the energy of the barrier on the  $T_1$  PES is approached and then exceeded.

Table 1 also reports the  $\langle E_{\text{vib}} \rangle / E_{\text{avil}}$  values for the HCO products formed following excitation into various  $2^2 4^3$  and  $2^3 4^1$  initial states. The correlation between these values and the associated  $\langle E_{\text{rot}} \rangle / E_{\text{avil}}$  values is shown in Figure 6. For the  $2^3 4^1$  state, the rotational level ( $1_{10}$ ) previously identified as reacting predominantly via the  $T_1$  mechanism also yields significantly less population in the  $v_3 = 1$  level of HCO. Nonetheless, the trend in Figure 6 shows that the triplet channel produces less overall vibrational and rotational excitation than does the singlet channel. In addition, the amount of rotational excitation is about twice that of vibrational excitation for both mechanisms.

Vibrational energy data for the lower-lying  $2^2 4^3$  state are less complete. However, the three  $2^2 4^3$  points lie significantly below the  $2^3 4^1$  data, implying less vibrational excitation following dissociation from the lower-lying state. The  $2^2 4^3$  state lies only  $125 \text{ cm}^{-1}$  above the threshold for producing HCO ( $v_3 = 1$ ), whereas  $2^3 4^1$  lies about  $400 \text{ cm}^{-1}$  above the threshold. Therefore, the lower vibrational population for  $2^2 4^3$  is likely to be an energy constraint rather than a dynamical one.

## Conclusions

Two complementary techniques have been used to determine PSDs for  $\text{H}_2\text{CO}$  photolysis to  $\text{H} + \text{HCO}$  via both singlet and triplet mechanisms. Each technique has its own strengths and limitations, and neither, on its own, can provide quantitative PSDs across the  $v$ ,  $N$ ,  $K_a$ ,  $K_c$ ,  $J$  states of HCO. In this work, we have combined the techniques using the same initial  $\text{H}_2\text{CO}$  rovibronic states. In doing so, we used LIF to validate the fitting procedure for overall  $N$  distributions from the Rydberg tagging experiments. The Rydberg tagging data led to a comprehensive analysis of the  $K_a$  distributions showing that HCO born on  $S_0$  has a statistical PSD, modeled well by phase space theory. HCO born on  $T_1$  shows a truncated  $K_a$  distribution, in good agreement

with recent QCT calculations. Complete information on rotational populations has allowed us to calculate the overall energy partitioning into rotational degrees of freedom, which is  $\sim 25\text{--}30\%$  for many initial states, lower for dissociation via the  $T_1$  mechanism and higher for the  $S_0$  mechanism.

Rydberg tagging is unable to provide rotational resolution in the  $v_3 = 1$  state, which is also accessible at these energies. LIF can provide the rotational resolution for  $v_3 = 1$  products but is less reliable in comparing the  $v_3 = 1$  rotational populations with those of  $v = 0$  and unable to provide overall vibrational populations. However, Rydberg tagging can provide the overall vibrational population ratio and thereby provide an independent calibration to scale the LIF data. Therefore, we are able to report accurate  $v = 0$  and  $v_3 = 1$  rotational distributions and can extract the energy partitioning into vibrational degrees of freedom. For the  $2^3 4^1$  state, product vibrational excitation was, on average,  $\sim 15\%$  of the available energy, or about half the average level of rotational excitation. Dissociation via the lower-lying  $2^4 3$  state produces less vibrational excitation but similar rotational excitation. This is a consequence of  $2^4 3$  lying only  $125\text{ cm}^{-1}$  above the energetic threshold for forming  $v_3 = 1$  products, which severely limits the number of available product rotational product states.

**Acknowledgment.** The Canadian authors acknowledge funding from NSERC and the Association of Commonwealth Universities. The U.K. authors would like to thank EPSRC for the award of the LASER portfolio grant, and the Australian authors gratefully acknowledge support from the ARC (DP0772006).

## References and Notes

- (1) Moore, C. B.; Weishaar, J. C. *Annu. Rev. Phys. Chem.* **1983**, *34*, 525.
- (2) Zare, R. N. *Science* **2006**, *311*, 1383.

- (3) Townsend, D.; Lahankar, S. A.; Lee, S. K.; Chambreau, S. D.; Suits, A. G.; Zhang, X.; Rheinecker, J.; Harding, L. B.; Bowman, J. M. *Science* **2004**, *306*, 1158.
- (4) Lahankar, S. A.; Chambreau, S. F.; Zhang, X.; Bowman, J. M.; Suits, A. G. *J. Chem. Phys.* **2007**, *126*, 044314.
- (5) Terentis, A. C.; Kable, S. H. *Chem. Phys. Lett.* **1996**, *258*, 626.
- (6) Terentis, A. C.; Waugh, S. E.; Metha, G. F.; Kable, S. H. *J. Chem. Phys.* **1998**, *108*, 3187.
- (7) Yin, H.-M.; Nauta, K.; Kable, S. H. *J. Chem. Phys.* **2005**, *122*, 194312.
- (8) Chuang, M.-C.; Foltz, M. F.; Moore, C. B. *J. Chem. Phys.* **1987**, *76*, 3855.
- (9) Dulligan, M.; Tuchler, M. F.; Zhang, J.; Kolessov, A.; Wittig, C. *Chem. Phys. Lett.* **1997**, *276*, 84.
- (10) Valachovic, L. R.; Tuchler, M. F.; Dulligan, M.; Droz-Georget, Th.; Zyrianov, M.; Kolessov, A.; Reisler, H.; Wittig, C. *J. Chem. Phys.* **2000**, *112*, 2752.
- (11) Yamaguchi, Y.; Wesolowski, S. S.; Van Huis, T. J.; Schaefer, H. F., III. *J. Chem. Phys.* **1998**, *108*, 5281.
- (12) Yin, H.-M.; Kable, S. H.; Zhang, X.; Bowman, J. M. *Science* **2006**, *311*, 1443.
- (13) Yin, H.-M.; Rowling, S. J.; Büll, A.; Kable, S. H. *J. Chem. Phys.* **2007**, *127*, 064302.
- (14) Hopkins, W. S.; Loock, H.-P.; Cronin, B.; Nix, M. G. D.; Devine, A. L.; Dixon, R. N.; Ashfold, M. N. R. *J. Chem. Phys.* **2007**, *127*, 064301.
- (15) Lee, S.-H.; Chen, I.-C. *J. Chem. Phys.* **1995**, *103*, 104.
- (16) Schnieder, L.; Meier, W.; Welge, K. H.; Ashfold, M. N. R.; Western, C. M. *J. Chem. Phys.* **1990**, *92*, 7027.
- (17) Cronin, B.; Devine, A. L.; Nix, M. G. D.; Ashfold, M. N. R. *Phys. Chem. Chem. Phys.* **2006**, *8*, 3440.
- (18) Blake, G. A.; Sastry, K. V. L. N.; Delucia, F. C. *J. Chem. Phys.* **1984**, *8*, 95.
- (19) Shiu, Y. J.; Chen, I.-C. *J. Mol. Spectrosc.* **1994**, *165*, 457.
- (20) Johns, J. W. C.; McKellar, A. R. W.; Riggall, M. *J. Chem. Phys.* **1977**, *67*, 2427.
- (21) Yin, H.-M.; Kable, S. H. *J. Mol. Spectrosc.* **2006**, *237*, 163.
- (22) Sears, T. J. *Comput. Phys. Commun.* **1984**, *34*, 123.
- (23) Lee, S.-H.; Chen, I.-C. *J. Chem. Phys.* **1996**, *105*, 4597.
- (24) Hunter, M.; Reid, S. A.; Robie, D. C.; Reisler, H. *J. Chem. Phys.* **1993**, *99*, 1093.

JP8021826